

Hierarchy of Ideal Flatbands in Chiral Twisted Multilayer Graphene Models

Jie Wang^{1,*} and Zhao Liu^{2,†}

¹Center for Computational Quantum Physics, Flatiron Institute, 162 5th Avenue, New York, NY 10010, USA

²Zhejiang Institute of Modern Physics, Zhejiang University, Hangzhou 310027, China

We propose models of twisted multilayer graphene that exhibit exactly flat Bloch bands with arbitrary Chern numbers and ideal band geometries. The models are constructed by twisting two sheets of Bernal-stacked multiple graphene layers with only inter-sublattice couplings. Analytically we show that flatband wavefunctions in these models exhibit a momentum space holomorphic character, leading to ideal band geometries. We also explicitly demonstrate a generic “wavefunction exchange” mechanism that generates the high Chern number of these ideal flatbands. The ideal band geometries and high Chern numbers of the flatbands imply the possibility of hosting exotic fractional Chern insulators which do not have analogues in continuum Landau levels. We numerically verify that these exotic fractional Chern insulators are model states for short-range interactions, characterized by exact ground-state degeneracies at zero energy and infinite particle-cut entanglement gaps.

Introduction.—The intrinsic topological and geometric properties of Bloch wavefunctions are crucial to the interacting phenomena in narrow-band systems such as Moiré materials [1–3] where electrons’ kinetic energy are quenched. The band topology enriches the possible many-body phase diagram [4–6]. On the other hand, the band geometry determines the actual stabilities of various many-body states [7].

As a representative example, twisted bilayer graphene (TBG) has two nearly flatbands of Chern number $\mathcal{C} = \pm 1$ at charge neutrality. Recently fractional Chern insulators (FCIs) [4–6] are theoretically predicted and experimentally observed in TBG flatbands [8–11]. One important factor to the stability of FCIs in this system is due to the ideal geometry of the flatbands in the fixed point chiral limit [12, 13], where each flatband’s Berry curvature $\Omega_{\mathbf{k}}$ is non-vanishing and strictly proportional to its Fubini-Study metric $g_{\mathbf{k}}^{ab}$ by a constant determinant-one matrix ω^{ab} [14–16]:

$$g_{\mathbf{k}}^{ab} = \omega^{ab} \Omega_{\mathbf{k}}, \quad \Omega_{\mathbf{k}} \neq 0 \quad \text{for } \forall \mathbf{k}, \quad (1)$$

where $a, b = x, y$ labels spatial coordinates. The ideal band geometry Eq. (1) implies the Bloch wavefunctions of the chiral TBG (cTBG) flatbands exhibit a momentum space holomorphic character [17, 18], in analogy to the real space holomorphic wavefunction in the conventional lowest Landau level (LLL). Such exact position-momentum duality leads to the existence of model FCIs in the cTBG flatbands as the exact zero-energy ground states of short-range interactions which are stable against the spatial fluctuation of band geometries [14, 16].

The ideal flatbands are special cases of the Kähler band [19–21] when the Kähler structure [22] is spatially constant. There is so far a glaring lack of microscopic models realizing ideal flatbands of high Chern numbers (high- \mathcal{C}). Compared with $|\mathcal{C}| = 1$ bands, high- \mathcal{C} bands are topologically different [23–25] and may support many-body phases without LL analogues [26–33]. In this work, we fill this void and propose a systematic construc-

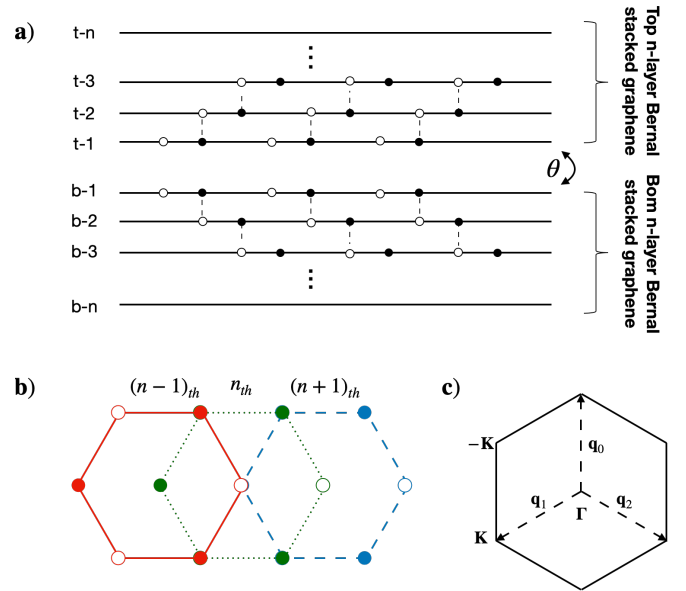


FIG. 1. (a) Geometry of our AB-AB stacking multi-layered model, which consists of n layers of Bernal stacked graphene on top and bottom sheets, respectively, with a relative small twisted angle θ in the middle. Here the solid and empty dots represent the A and B sublattice, respectively. (b) Illustration of the Bernal stacking structure in three consecutive layers. (c) The Moiré Brillouin zone with Dirac points $\pm \mathbf{K}$ and useful momentum vectors $\mathbf{q}_{0,1,2}$.

tion of microscopic models with relevance to Moiré materials. Our models are based on two sheets of n -layer Bernal stacked graphene which are twisted by a small angle and put in the chiral limit. Our hierarchy scheme starts with cTBG as the parent, and includes the chiral twisted double bilayer graphene (cTDBG) as the next descendant [34–36]. We show exactly flat bands existing at charge neutrality of our models, and we analytically and mathematically prove their ideal band geometry and exotic band topology. We also numerically show that

lattice-specific FCIs without LLL analogues are stable in these ideal flatbands as they appear as the exact zero-energy ground states of short-range interactions, paving the way towards understanding their stability against inhomogeneous band geometries.

Multilayer Chiral Model.—We consider two sheets of n -layer Bernal stacked graphene twisted by a small angle θ , as illustrated in Fig. 1. We focus on a single valley of the system [37–39] and take the chiral limit [12] by keeping only the inter-sublattice hopping between adjacent layers, such that the Hamiltonian of our model takes an off-diagonal form in the sublattice basis

$$H_n = (\Phi^\dagger \ \Xi^\dagger) \begin{pmatrix} \mathcal{D}_1 & \\ & \mathcal{D}_n \end{pmatrix} \begin{pmatrix} \Phi \\ \Xi \end{pmatrix}, \quad (2)$$

where the basis Φ and Ξ are fully sublattice- A and B polarized. We organize Φ (and Ξ) by layers, such that $\Phi = (\phi_1, \phi_2, \dots, \phi_n)^T$ where $\phi_i = (\phi_i^b, \phi_i^t)^T$ contains the sublattice- A components of the i th layer in the bottom sheet and the i th layer in the top sheet (Fig. 1). In this basis, we have

$$\mathcal{D}_n = \begin{pmatrix} \mathcal{D}_1 & t_1 T_+ & & & \\ t_1 T_- & h_D & t_2 T_+ & & \\ & t_2 T_- & h_D & \ddots & \\ & & \ddots & & t_{n-1} T_+ \\ & & & t_{n-1} T_- & h_D \end{pmatrix},$$

where h_D and \mathcal{D}_1 are respectively the Dirac Hamiltonian of a free-standing monolayer graphene and the Hamiltonian of cTBG [12], given by

$$h_D = \begin{pmatrix} -i\partial & \\ & -i\partial \end{pmatrix}, \quad \mathcal{D}_1 = \begin{pmatrix} -i\partial & U_{-\phi} \\ U_\phi^* & -i\partial \end{pmatrix}. \quad (3)$$

Here $U_\phi = \alpha (e^{-iq_0 \cdot \mathbf{r}} + e^{i\phi} e^{-iq_1 \cdot \mathbf{r}} + e^{-i\phi} e^{-iq_2 \cdot \mathbf{r}})$ with $\phi = 2\pi/3$ and $\alpha \propto \sin^{-1}(\theta/2)$ [12], $\partial = (\partial_x - i\partial_y)/\sqrt{2}$, and the momenta $\mathbf{q}_{0,1,2}$ are illustrated in Fig. 1(c). The twist angle θ is set as the magic angle of cTBG [12]. We only retain the strongest tunneling in the Bernal stacking structure [Fig. 1(b)], which couples electrons in n th layer sublattice- A to those in $(n+1)$ th layer sublattice- B by the real tunneling strength t_n . See Fig. 1(a) for an illustration. Under this assumption, the interlayer coupling matrices T_\pm are

$$T_+ = \begin{pmatrix} 1 & 0 \\ 0 & 0 \end{pmatrix}, \quad T_- = \begin{pmatrix} 0 & 0 \\ 0 & 1 \end{pmatrix}. \quad (4)$$

Details of the model Hamiltonian are left to the supplementary material (SM).

The model Eq. (2) preserves the translation $\mathcal{V}_{1,2}$ and the three-fold rotation \mathcal{C}_3 symmetries, but it breaks the time-reversal \mathcal{T} and the two-fold rotation \mathcal{C}_2 as they interchange valleys [40–44]. The combination $\mathcal{C}_2\mathcal{T}$ is also

Chiral Symmetry	Intravalley Inversion Symmetry
$\sigma_z = \begin{pmatrix} 1 & \\ & -1 \end{pmatrix}$	$\mathcal{I} = \begin{pmatrix} \mathcal{P} & \\ & -\mathcal{P} \end{pmatrix} \sigma_x \mathcal{K}$
$\{H, \sigma_z\} = 0$	$[H, \mathcal{I}] = 0$

TABLE I. Exact emergent symmetries of the model, which include the chiral symmetry σ_z and the intra-valley inversion symmetry \mathcal{I} . The combination of both symmetries implies that the spectrum is not only particle-hole symmetric but also \mathbf{k} to $-\mathbf{k}$ symmetric within the same valley. The matrices above are written in the sublattice basis Φ and Ξ .

broken by the Bernal-stacking unless $n = 1$. Besides the lattice symmetries, the model has two exact emergent symmetries: the chiral symmetry σ_z and the intravalley inversion symmetry \mathcal{I} . As defined in Table I, they respectively imply a particle-hole symmetry and an inversion symmetry to the spectrum and eigen-wavefunctions. In the definition of \mathcal{I} , \mathcal{K} is the complex conjugation operator and $\mathcal{P} = \text{diag}(\tau_y, -\tau_y, \dots, (-)^{n-1}\tau_y)$, where τ_y acts on the i th bottom and top layers. Throughout this work, we use Pauli matrix σ for sublattice and τ for layers. Note that the intravalley inversion \mathcal{I} reduces to the known form for cTBG [15] when the $\mathcal{C}_2\mathcal{T}$ symmetry is restored [45]. Ignoring the negligible small twist angle effect, \mathcal{I} is identical to the approximate unitary particle-hole symmetry [43, 46–51].

Twisted bilayer graphene.—We now proceed to demonstrate the existence of ideal flatbands in our model. We start with reviewing the simplest case with $n = 1$, i.e., cTBG. It has been shown in Refs. [12, 14, 15, 52–56] that cTBG is an exactly solvable model exhibiting $|\mathcal{C}| = 1$ dispersionless bands at charge neutrality with ideal band geometry when it is twisted by the magic angle. The wavefunctions of these ideal flatbands are found to have an exact connection [15] (up to a normalization factor) to the LLL wavefunction $\Phi_{\mathbf{k}}^{\text{LLL}}(\mathbf{r})$ [57–60]:

$$\Phi_1 = \begin{pmatrix} \phi_1 \\ \phi'_1 \end{pmatrix} = \begin{pmatrix} i\mathcal{G}(\mathbf{r}) \\ \eta\mathcal{G}(-\mathbf{r}) \end{pmatrix} \Phi_{\mathbf{k}}^{\text{LLL}}(\mathbf{r}), \quad (5)$$

where $\eta = \pm 1$ is the intravalley inversion eigenvalue and the \mathbf{k} -independent $\mathcal{G}(\mathbf{r})$ can be interpreted as a quantum Hall wave function in a magnetic field oppositely directed to that of $\Phi_{\mathbf{k}}^{\text{LLL}}(\mathbf{r})$ [15]. This connection to the LLL wavefunction implies that its cell periodic wavefunction $e^{-i\mathbf{k} \cdot \mathbf{r}} \Phi_{1,\mathbf{k}}$ is holomorphic in $k = (k_x + ik_y)/\sqrt{2}$ ignoring the normalization factor [61]. For any Bloch wavefunction satisfying this property, Eq. (1) is automatically satisfied [14, 16, 17, 62]. The unit Chern number and ideal band geometry thereby make cTBG an exact \mathbf{k} -space dual of the LLL with nontrivial curvature [16].

Twisted double bilayer graphene.—We now discuss the first nontrivial case, i.e., $n = 2$ cTDBG. It has been no-

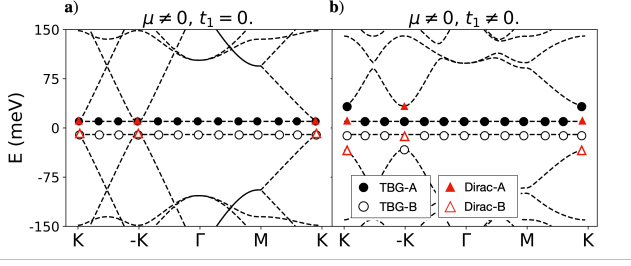


FIG. 2. High- C bands generated by the “wavefunction exchange” mechanism. In (a) and (b), we show the sublattice polarization properties of the cTBG (black circles) and Dirac wavefunctions (red triangles) before and after turning on an infinitesimal interlayer coupling t_1 , respectively, where the solid/empty markers represent sublattice- A/B polarization, respectively. The Dirac wavefunction interchanges with the cTBG wavefunction at $\pm\mathbf{K}$, which punctures a zero to cTBG wavefunction and increases the Chern number by one. This is the generic mechanism that generates high Chern number in our model.

ticed that cTDBG has two exactly flat bands at charge neutrality [34]. Despite of this observation, the wavefunction, topology and geometry of these flatbands were ignored before, which we will analyze in detail below. Since the two flatbands are sublattice polarized and related by \mathcal{I} , without loss of generality we focus on the sublattice- A flatband wavefunction Φ_2 which is the zero mode of \mathcal{D}_2^\dagger . We denote Φ_2 as $(\Phi_1^T, \phi_2, \phi_3)^T$ where $\Phi_1 = (\phi_1, \phi_1')^T$ is a two-component layer spinor. Component-wisely, the zero mode equation $\mathcal{D}_2^\dagger \Phi_2 = 0$ becomes

$$\mathcal{D}_1^\dagger \Phi_1 + t_1 (0, \phi_3)^T = 0, \quad -i\bar{\partial}\phi_3 = 0, \quad (6)$$

$$-i\bar{\partial}\phi_2 + t_1\phi_1 = 0. \quad (7)$$

The solutions of these equations are $\phi_3 = 0$ [63] and Φ_1 being the zero mode of cTBG up to a normalization factor $N_{\mathbf{k}}$. As only \mathcal{D}_1^\dagger depends on the twist angle, the magic angles of cTDBG and cTBG are identical, at which the bands at charge neutrality are exactly flat.

The only nontrivial zero mode equation for cTDBG is Eq. (7) which governs the essential properties of band topology, band geometry and interacting physics through ϕ_2 . To prove the ideal band geometry of the magic angle cTDBG, we merely need to show the cell-periodic part of ϕ_2 ($u_2 \equiv e^{-i\mathbf{k}\cdot\mathbf{r}}\phi_2$) is holomorphic in \mathbf{k} up to a normalization, since Φ_1 , as the zero mode of cTBG, is already proved to satisfy this condition [14]. The key observation is that Eq. (7) only has anti-holomorphic derivative $\bar{\partial}$, thereby the differential equation for u_2 , $(\bar{\partial} + i\mathbf{k})u_2 = -it_1u_1$, depends only on \mathbf{k} but not on \mathbf{k} . Then $\bar{\partial}_k u_2 = 0$ follows immediately from the fact that $\bar{\partial}_k u_1 = 0$. Here $u_1 \equiv e^{-i\mathbf{k}\cdot\mathbf{r}}\phi_1$.

Next we discuss band topology. While it is known that the AB-AB Bernal-stacking structure can support high Chern number [34, 64], here we provide a proof which highlights the analytical structure of the cTDBG flat-

band wavefunction. For convenience, in the following we assume a small hexagonal-boron-nitride potential $\mu > 0$ to split the degeneracy of the two cTDBG flatbands and meanwhile preserve their sublattice polarization.

We start by considering the limit of zero interlayer coupling $t_1 = 0$. In this case, in the low-energy regime there are two exactly flat bands ($\phi_{\text{cTBG}}, \chi_{\text{cTBG}}$) originating from the inner cTBG layers and two Dirac bands ($\phi_{\text{D}}, \chi_{\text{D}}$) from the outermost layers. The cTBG and the Dirac bands are degenerate at the Dirac points $\pm\mathbf{K}$, as shown in Fig. 2(a). In the following, we focus on the Dirac point \mathbf{K} to examine the gap opening mechanism as the physics at $-\mathbf{K}$ is simply implied by the intravalley inversion. The \mathbf{K} point wavefunctions ($\phi_{\text{cTBG}}, \phi_{\text{D}}$) at energy μ are sublattice- A polarized and ($\chi_{\text{cTBG}}, \chi_{\text{D}}$) at energy $-\mu$ are sublattice- B polarized [Fig. 2(a)]. We further note that ($\phi_{\text{D}}, \chi_{\text{D}}$) are also polarized in the bottom layer. Under this scenario, in the “(bottom, top)” layer basis we have

$$\begin{aligned} \phi_{\text{cTBG}} &= (\phi_1, \phi_1')^T, & \phi_{\text{D}} &= (1, 0)^T, \\ \chi_{\text{cTBG}} &= (\chi_1, \chi_1')^T, & \chi_{\text{D}} &= (1, 0)^T. \end{aligned} \quad (8)$$

We then turn on an infinitesimal t_1 and use the perturbation theory to study the change of band structure and wavefunctions. As the t_1 terms couple adjacent layers of opposite sublattices, the perturbation matrix elements within the four low-energy bands are

$$\langle \phi_{\text{cTBG}} | T_+ | \chi_{\text{D}} \rangle \neq 0, \quad \langle \chi_{\text{cTBG}} | T_- | \phi_{\text{D}} \rangle = 0, \quad (9)$$

where details of Eq. (8) and Eq. (9) can be found in SM.

Eq. (9) implies that χ_{cTBG} and ϕ_{D} are unperturbed at \mathbf{K} , but ϕ_{cTBG} and χ_{D} start to repel each other immediately after turning on t_1 . The net result is that a band gap is opened and the cTBG and Dirac bands at positive energy are effectively “exchanged” at \mathbf{K} [Fig. 2(b)], leaving $\Phi_{2,\mathbf{K}}$ to be $(0, 0, 1, 0)^T$. We find that $\Phi_{2,\mathbf{K}}$ remains $(0, 0, 1, 0)^T$ for arbitrary $t_1 \neq 0$ because the flatband energy stays at μ independent on t_1 . On the other hand, Eq. (6) dictates that first two components of Φ_2 is identical to the cTBG wavefunction up to a normalization factor $N_{\mathbf{k}}$. Thus our analysis shows $N_{\mathbf{k}}$ must be zero at \mathbf{K} ; how fact $N_{\mathbf{k}}$ decays to zero when \mathbf{k} approaching \mathbf{K} is determined by $|t_1|$.

This “wavefunction exchange” increases the flatband Chern number by one. The Chern number measures the discontinuity of the Bloch wavefunction which resides either at the boundary or in the bulk of the Brillouin zone [65, 66]. In our case, the discontinuities occurs at the Brillouin zone boundary and the Dirac point. Since \mathcal{C} is an invariant, it is sufficient to work with an infinitesimal $|t_1|$. In this case, $N_{\mathbf{k}} = 1$ except near the Dirac points, and one can choose the Brillouin zone boundary to avoid the Dirac points such that the boundary contribution to \mathcal{C} is determined by cTBG wavefunction which equals to one. The vanishing of $N_{\mathbf{K}}$ is equivalent

as stating a pole singularity of the Dirac component ϕ_D at \mathbf{K} , which increases the Chern number by one following Ref. [17, 18]. We therefore proved the cTDBG flatband has Chern number two.

Hierarchy scheme.—The discussion of cTDBG ($n = 2$) can be straightforwardly generalized to arbitrary n . Given the zero mode wavefunction Φ_{n-1} of H_{n-1} , the zero mode of H_n must exist at the same magic angle, whose ansatz can be written as $\Phi_n^T = (\Phi_{n-1}^T, \phi_n, 0)$ and the zero-mode equation generalizing Eq. (7) is

$$-i\bar{\partial}\phi_n + t_{n-1}\phi_{n-1} = 0. \quad (10)$$

Since Eq. (10) only has anti-holomorphic derivatives, the cell-periodic part of ϕ_n is a holomorphic function of k as that of ϕ_{n-1} is. We therefore prove the ideal band geometry of Φ_n from the hierarchy construction. The band topology can also be analyzed by the same method. Starting with $t_{n-1} = 0$, $t_{i=1,\dots,n-2} \neq 0$, the H_n at magic angle consists of two sublattice polarized flatbands originating from Φ_{n-1} which are degenerate with the two outermost freestanding Dirac bands at Dirac points. Finite but infinitesimal $|t_{n-1}|$ splits the degeneracy and “exchanges” the Φ_{n-1} with the Dirac band leaving $\Phi_{n,\mathbf{K}}$ to be $(0, \dots, 0, 1, 0)^T$. This does not alter the boundary contribution to \mathcal{C} but generates an unavoidable bulk pole singularity and increases \mathcal{C} by one. We therefore prove the Chern number of our flatband is determined by the number of layers $\mathcal{C} = n$, and all the flatbands have ideal band geometry satisfying Eq. (1).

Exact fractional Chern insulators.—We now examine the interacting physics in the ideal flatband of our model. As the pertinent band is exactly flat, we drop the kinetic energy and project the interaction into the ideal flatband. The band filling factor ν is defined as $N/(N_1N_2)$ for N electrons and N_1, N_2 unit cells in the two primitive directions of the Moire pattern. As the many-body Hamiltonian preserves the total momentum, each eigenstate can be labeled by its total momentum (K_1, K_2) . In TBG, it has been numerically demonstrated that the $\mathcal{C} = 1$ flatband at the charge neutrality can host the lattice Laughlin FCIs at $\nu = 1/3$ [8–10]. In particular, the model $\nu = 1/3$ Laughlin state was found to be the exact zero-energy ground state at the chiral limit for the shortest ranged two-body interaction $H_{\text{int}} = \sum_{i<j} \delta''(\mathbf{r}_i - \mathbf{r}_j)$ [67].

In high- \mathcal{C} Bloch bands, robust FCIs were reported across various models [26–33]. Remarkably, in our ideal flatbands, we observe an *exact* $(2n+1)$ -fold degenerate zero-energy ground states for H_{int} , separated by a finite energy gap to excitations [Figs. 3(a) and 3(b) for $n = 2$ and $n = 3$]. Their particle-cut entanglement spectra (PES) [4], defined as the entanglement between subsystems of N_A and $N - N_A$ particles, are displayed in Figs. 3(c) and 3(d). The counting of low PES levels agrees with the expectation from FCI quasihole excitations. The high PES levels appear only above the machine error cut-off

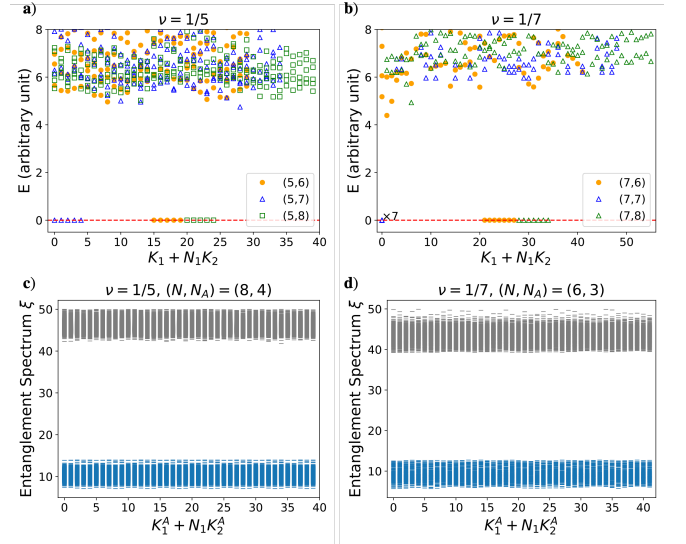


FIG. 3. Energy spectra and particle-cut entanglement spectra (PES) demonstrating exact model FCIs. (a) and (b): Energy spectra of the $H_{\text{int}} = \sum_{i<j} \delta''(\mathbf{r}_i - \mathbf{r}_j)$ interaction in the $\mathcal{C} = n$ ideal flatband at filling fraction $\nu = 1/(2n+1)$, where (a) is for $n = 2$ (cTDBG) and (b) is for $n = 3$ (cTDTG). An $(2n+1)$ -fold exactly degenerate ground states at zero energy are clearly observed. Lattice sizes $(N_1, N_2) = (2n+1, N)$ are given in the legends. The red dashed lines mark the zero energy and are used to guide the eyes. (c) and (d): PES for $N = 8$ and $N = 6$ particles. The grey levels above $\xi_c = |\ln(2^{-53})| \approx 36.7$ are machine noises. The number of low-energy PES levels is 17710 and 3248 in (c) and (d) respectively, agreeing with the FCI quasihole counting [26, 27]. The infinite entanglement gap strongly suggests the FCIs are model states.

$\xi_c \approx 36.7$, strongly suggesting an infinite PES gap and the exact zero modes are model FCIs.

Discussions.—We systematically construct models based on chiral twisted multilayered graphene sheets that exhibit exotic band topology and ideal band geometry without fine tunings [18, 21, 25]. The constructed flatband wavefunctions resemble the LLL through the position-momentum duality, but distinguishes from the LLL by exhibiting high Chern numbers. Numerically we found these flatbands harbor a large class of model FCIs characterized by the exact ground-state degeneracies and infinite PES gap. The ideal flatband and model FCIs have a wide range of immediate applications on uncovering the universal aspects of topological flatbands beyond the LLL limit, including for instance the band geometry tuned phase transitions [16, 68], geometric responses [69–71] and low-energy excitations [72–74].

There are a couple of open questions which deserve future studies. Uncovering more physical and mathematical structure of the single-particle wavefunction ϕ_n is an interesting direction. We noticed that the model FCIs are intrinsic to the outermost Dirac layer: further projecting H_{int} into the ϕ_n component of Φ_n changes the energies of

excited states but leaves the exact degenerate zero-energy ground states and the PES unaffected. This means ϕ_n alone could exhibit a “color-entangled” feature [28] which remains challenging to uncover analytically from the zero mode equation Eq. (10). Furthermore, a thorough understanding of the origin of the exact model FCIs is another important open problem. Exact model FCIs were also reported in the numerical studies of onsite interacting bosons in the Kapit-Mueller model [75, 76] and its variations [31]. Considering the band geometry of the Kapit-Mueller model was numerically found to be ideal [77], we anticipate the ideal band geometry also exist in the multilayered KM model [31], and the ideal band geometry may underline the fundamental reason to the frustration free nature of this large class of lattice-specific interacting Hamiltonians. A complete understanding may require a momentum space reformulation of the interacting problem and a careful study of the projected density operator algebra [17, 62, 72–74, 78].

J.W. is grateful to Bartholomew Andrews, Semyon Klevtsov, Nicolas Regnault and Ya-Hui Zhang for useful discussions. We acknowledge Jennifer Cano, Andrew J. Millis and Bo Yang for the collaboration on Chern number one ideal flatbands. Z.L. acknowledges Ahmed Abouelkomsan and Emil J. Bergholtz for the collaboration on related topics. We are grateful to Bartholomew Andrews and Jennifer Cano for reading the manuscript. Z.L. is supported by the National Key Research and Development Program of China through Grant No. 2020YFA0309200. The Flatiron Institute is a division of the Simons Foundation.

* jiewang@flatironinstitute.org

† zhaol@zju.edu.cn

- [1] E. Y. Andrei and A. H. MacDonald, *Nature Materials* **19**, 1265 (2020).
- [2] L. Balents, C. R. Dean, D. K. Efetov, and A. F. Young, *Nature Physics* **16**, 725 (2020).
- [3] D. M. Kennes, M. Claassen, L. Xian, A. Georges, A. J. Millis, J. Hone, C. R. Dean, D. N. Basov, A. N. Pasupathy, and A. Rubio, *Nature Physics* **17**, 155 (2021).
- [4] N. Regnault and B. A. Bernevig, *Phys. Rev. X* **1**, 021014 (2011).
- [5] S. A. Parameswaran, R. Roy, and S. L. Sondhi, *Comptes Rendus Physique* **14**, 816 (2013), topological insulators / Isolants topologiques.
- [6] E. J. BERGHOLTZ and Z. LIU, *International Journal of Modern Physics B* **27**, 1330017 (2013), <https://doi.org/10.1142/S021797921330017X>.
- [7] T. S. Jackson, G. Möller, and R. Roy, *Nature Communications* **6**, 8629 (2015).
- [8] A. Abouelkomsan, Z. Liu, and E. J. Bergholtz, *Phys. Rev. Lett.* **124**, 106803 (2020).
- [9] C. Repellin and T. Senthil, *Phys. Rev. Research* **2**, 023238 (2020).
- [10] C. Repellin, Z. Dong, Y.-H. Zhang, and T. Senthil, *Phys. Rev. Lett.* **124**, 187601 (2020).
- [11] Y. Xie, A. T. Pierce, J. M. Park, D. E. Parker, E. Khalaf, P. Ledwith, Y. Cao, S. H. Lee, S. Chen, P. R. Forrester, K. Watanabe, T. Taniguchi, A. Vishwanath, P. Jarillo-Herrero, and A. Yacoby, arXiv e-prints, arXiv:2107.10854 (2021), [arXiv:2107.10854](https://arxiv.org/abs/2107.10854) [cond-mat.mes-hall].
- [12] G. Tarnopolsky, A. J. Kruchkov, and A. Vishwanath, *Phys. Rev. Lett.* **122**, 106405 (2019).
- [13] O. Vafek and J. Kang, *Phys. Rev. Lett.* **125**, 257602 (2020).
- [14] P. J. Ledwith, G. Tarnopolsky, E. Khalaf, and A. Vishwanath, *Phys. Rev. Research* **2**, 023237 (2020).
- [15] J. Wang, Y. Zheng, A. J. Millis, and J. Cano, *Phys. Rev. Research* **3**, 023155 (2021).
- [16] J. Wang, J. Cano, A. J. Millis, Z. Liu, and B. Yang, arXiv e-prints, arXiv:2105.07491 (2021), [arXiv:2105.07491](https://arxiv.org/abs/2105.07491) [cond-mat.mes-hall].
- [17] M. Claassen, C. H. Lee, R. Thomale, X.-L. Qi, and T. P. Devereaux, *Phys. Rev. Lett.* **114**, 236802 (2015).
- [18] C. H. Lee, M. Claassen, and R. Thomale, *Phys. Rev. B* **96**, 165150 (2017).
- [19] T. Ozawa and B. Mera, *Phys. Rev. B* **104**, 045103 (2021).
- [20] B. Mera and T. Ozawa, *Phys. Rev. B* **104**, 045104 (2021).
- [21] B. Mera and T. Ozawa, arXiv e-prints, arXiv:2107.09039 (2021), [arXiv:2107.09039](https://arxiv.org/abs/2107.09039) [cond-mat.mes-hall].
- [22] M. R. Douglas and S. Klevtsov, *Communications in Mathematical Physics* **293**, 205 (2009).
- [23] M. Trescher and E. J. Bergholtz, *Phys. Rev. B* **86**, 241111 (2012).
- [24] S. Yang, Z.-C. Gu, K. Sun, and S. Das Sarma, *Phys. Rev. B* **86**, 241112 (2012).
- [25] A. Kruchkov, arXiv e-prints, arXiv:2105.14672 (2021), [arXiv:2105.14672](https://arxiv.org/abs/2105.14672) [cond-mat.str-el].
- [26] Z. Liu, E. J. Bergholtz, H. Fan, and A. M. Läuchli, *Phys. Rev. Lett.* **109**, 186805 (2012).
- [27] A. Sterdyniak, C. Repellin, B. A. Bernevig, and N. Regnault, *Phys. Rev. B* **87**, 205137 (2013).
- [28] Y.-L. Wu, N. Regnault, and B. A. Bernevig, *Phys. Rev. Lett.* **110**, 106802 (2013).
- [29] G. Möller and N. R. Cooper, *Phys. Rev. Lett.* **115**, 126401 (2015).
- [30] Y.-H. Wu, J. K. Jain, and K. Sun, *Phys. Rev. B* **91**, 041119 (2015).
- [31] J. Behrmann, Z. Liu, and E. J. Bergholtz, *Phys. Rev. Lett.* **116**, 216802 (2016).
- [32] B. Andrews and G. Möller, *Phys. Rev. B* **97**, 035159 (2018).
- [33] B. Andrews, T. Neupert, and G. Möller, *Phys. Rev. B* **104**, 125107 (2021).
- [34] F. Haddadi, Q. Wu, A. J. Kruchkov, and O. V. Yazyev, *Nano Letters*, *Nano Letters* **20**, 2410 (2020).
- [35] J. Y. Lee, E. Khalaf, S. Liu, X. Liu, Z. Hao, P. Kim, and A. Vishwanath, *Nature Communications* **10**, 5333 (2019).
- [36] Z. Liu, A. Abouelkomsan, and E. J. Bergholtz, *Phys. Rev. Lett.* **126**, 026801 (2021).
- [37] R. Bistritzer and A. H. MacDonald, *Proceedings of the National Academy of Sciences* **108**, 12233 (2011), <https://www.pnas.org/content/108/30/12233.full.pdf>.
- [38] J. M. B. Lopes dos Santos, N. M. R. Peres, and A. H. Castro Neto, *Phys. Rev. B* **86**, 155449 (2012).
- [39] J. M. B. Lopes dos Santos, N. M. R. Peres, and A. H. Castro Neto, *Phys. Rev. Lett.* **99**, 256802 (2007).

- [40] E. J. Mele, *Phys. Rev. B* **84**, 235439 (2011).
- [41] H. C. Po, L. Zou, A. Vishwanath, and T. Senthil, *Phys. Rev. X* **8**, 031089 (2018).
- [42] L. Zou, H. C. Po, A. Vishwanath, and T. Senthil, *Phys. Rev. B* **98**, 085435 (2018).
- [43] Z. Song, Z. Wang, W. Shi, G. Li, C. Fang, and B. A. Bernevig, *Phys. Rev. Lett.* **123**, 036401 (2019).
- [44] N. Bultinck, E. Khalaf, S. Liu, S. Chatterjee, A. Vishwanath, and M. P. Zaletel, *Phys. Rev. X* **10**, 031034 (2020).
- [45] Ref. [15] defined the intravalley inversion as $\mathcal{I}' \equiv \text{diag}(\mathcal{P}, -\mathcal{P})$ which differs from \mathcal{I} of Table. I by $\sigma_x \mathcal{K}$. The $\sigma_x \mathcal{K}$ is a combination of $\mathcal{C}_2 \mathcal{T}$ and $\mathbf{r} \rightarrow -\mathbf{r}$. Since H_1 is $\mathcal{C}_2 \mathcal{T}$ invariant, the commutation $[H_1, \mathcal{I}] = 0$ yields the relation $\mathcal{I}' H_1(\mathbf{r}) \mathcal{I}'^\dagger = H_1(-\mathbf{r})$ noticed in Ref. [15].
- [46] B. A. Bernevig, Z.-D. Song, N. Regnault, and B. Lian, *Phys. Rev. B* **103**, 205411 (2021).
- [47] Z.-D. Song, B. Lian, N. Regnault, and B. A. Bernevig, *Phys. Rev. B* **103**, 205412 (2021).
- [48] B. A. Bernevig, Z.-D. Song, N. Regnault, and B. Lian, *Phys. Rev. B* **103**, 205413 (2021).
- [49] B. Lian, Z.-D. Song, N. Regnault, D. K. Efetov, A. Yazdani, and B. A. Bernevig, *Phys. Rev. B* **103**, 205414 (2021).
- [50] B. A. Bernevig, B. Lian, A. Cowsik, F. Xie, N. Regnault, and Z.-D. Song, *Phys. Rev. B* **103**, 205415 (2021).
- [51] F. Xie, A. Cowsik, Z.-D. Song, B. Lian, B. A. Bernevig, and N. Regnault, *Phys. Rev. B* **103**, 205416 (2021).
- [52] S. Becker, M. Embree, J. Wittsten, and M. Zworski, “Mathematics of magic angles in a model of twisted bilayer graphene,” (2020), [arXiv:2008.08489 \[math-ph\]](https://arxiv.org/abs/2008.08489).
- [53] S. Becker, M. Embree, J. Wittsten, and M. Zworski, *Phys. Rev. B* **103**, 165113 (2021).
- [54] Y. Ren, Q. Gao, A. H. MacDonald, and Q. Niu, *Phys. Rev. Lett.* **126**, 016404 (2021).
- [55] F. K. Popov and A. Milekhin, *Phys. Rev. B* **103**, 155150 (2021).
- [56] G. G. Naumis, L. A. Navarro-Labastida, E. Aguilar-Méndez, and A. Espinosa-Champo, *Phys. Rev. B* **103**, 245418 (2021).
- [57] J. Wang, S. D. Geraedts, E. H. Rezayi, and F. D. M. Haldane, *Phys. Rev. B* **99**, 125123 (2019).
- [58] F. D. M. Haldane, *Journal of Mathematical Physics* **59**, 071901 (2018), <https://doi.org/10.1063/1.5042618>.
- [59] S. D. Geraedts, J. Wang, E. H. Rezayi, and F. D. M. Haldane, *Phys. Rev. Lett.* **121**, 147202 (2018).
- [60] J. Wang, *Phys. Rev. Lett.* **122**, 257203 (2019).
- [61] Following Refs. [57–60], the LLL wavefunction $\Phi_{\mathbf{k}}^{\text{LLL}}(\mathbf{r})$ can be expressed in terms of the modified Weierstrass sigma function $\sigma(z)$ as $e^{ik^*z} \sigma(z + ik) e^{-\frac{1}{2}(|z|^2 + |k|^2)}$. Its “cell-periodic” part $u_{\mathbf{k}}^{\text{LLL}}(\mathbf{r}) \equiv e^{-i\mathbf{k} \cdot \mathbf{r}} \Phi_{\mathbf{k}}^{\text{LLL}}(\mathbf{r})$ is holomorphic in k ignoring the normalization factor.
- [62] R. Roy, *Phys. Rev. B* **90**, 165139 (2014).
- [63] ϕ_3 cannot be a non-zero constant, which violates the Bloch translational symmetry.
- [64] Y.-H. Zhang, D. Mao, Y. Cao, P. Jarillo-Herrero, and T. Senthil, *Phys. Rev. B* **99**, 075127 (2019).
- [65] D. J. Thouless, *Journal of Physics C: Solid State Physics* **17**, L325 (1984).
- [66] D. J. Thouless, M. Kohmoto, M. P. Nightingale, and M. den Nijs, *Phys. Rev. Lett.* **49**, 405 (1982).
- [67] F. D. M. Haldane, *Phys. Rev. Lett.* **51**, 605 (1983).
- [68] B. Andrews, M. Mohan, and T. Neupert, *Phys. Rev. B* **103**, 075132 (2021).
- [69] F. D. M. Haldane, *Phys. Rev. Lett.* **107**, 116801 (2011).
- [70] T. Can, M. Laskin, and P. Wiegmann, *Phys. Rev. Lett.* **113**, 046803 (2014).
- [71] S. Klevtsov and P. Wiegmann, *Phys. Rev. Lett.* **115**, 086801 (2015).
- [72] S. M. Girvin, A. H. MacDonald, and P. M. Platzman, *Phys. Rev. B* **33**, 2481 (1986).
- [73] S. M. Girvin, A. H. MacDonald, and P. M. Platzman, *Phys. Rev. Lett.* **54**, 581 (1985).
- [74] C. Repellin, T. Neupert, Z. Papić, and N. Regnault, *Phys. Rev. B* **90**, 045114 (2014).
- [75] E. Kapit and E. Mueller, *Phys. Rev. Lett.* **105**, 215303 (2010).
- [76] J. Dong and E. J. Mueller, *Phys. Rev. A* **101**, 013629 (2020).
- [77] D. Varjas, A. Abouelkomsan, K. Yang, and E. J. Bergholtz, *arXiv e-prints*, [arXiv:2107.06902](https://arxiv.org/abs/2107.06902) (2021), [arXiv:2107.06902 \[cond-mat.str-el\]](https://arxiv.org/abs/2107.06902).
- [78] E. Dobardžić, M. V. Milovanović, and N. Regnault, *Phys. Rev. B* **88**, 115117 (2013).

— APPENDIX —

Chiral Hamiltonian

In this section, we discuss the details of the cTDBG Hamiltonian. The generalization to arbitrary n is straightforward. In the basis (Dirac bottom, TBG bottom, TBG top, Dirac top), the chiral Hamiltonian is given by,

$$h_0(\mathbf{r}) = \begin{pmatrix} \sigma_{-\theta/2}(-i\nabla - \mathbf{K}_+^b) & T_0 & 0 & 0 \\ T_0^\dagger & \sigma_{-\theta/2}(-i\nabla - \mathbf{K}_+^b) & T_\theta(\mathbf{r}) & 0 \\ 0 & T_\theta^\dagger(\mathbf{r}) & \sigma_{+\theta/2}(-i\nabla - \mathbf{K}_+^t) & T_0 \\ 0 & 0 & T_0^\dagger & \sigma_{+\theta/2}(-i\nabla - \mathbf{K}_+^t) \end{pmatrix}, \quad (11)$$

where the parameters are chosen as those in the standard Bistritzer-MacDonald model. $\mathbf{K}_{b,t}$ are respectively the Moiré Dirac point contributed from the bottom and top layer. Concrete values of the parameters can be found for

instance in the appendix of Refs. [8, 36]. In the above Hamiltonian,

$$T_0 = \begin{pmatrix} 0 & 0 \\ t_1 & 0 \end{pmatrix}, \quad T_\theta^\dagger(\mathbf{r}) = \sum_{j=0}^2 T_{j+1} e^{-i(\mathbf{q}_0 - \mathbf{q}_j) \cdot \mathbf{r}}, \quad T_{j+1} = \omega_1 e^{i(2\pi/3)j\sigma_z} \tau_x e^{-i(2\pi/3)j\sigma_z}. \quad (12)$$

Following Ref. [12], we perform unitary transformations to remove the $\mathbf{K}_{b/t}$ and θ dependence:

$$\begin{aligned} h_0(\mathbf{r}) &= \mathcal{M} h_1(\mathbf{r}) \mathcal{M}^\dagger, \quad \mathcal{M} = \mathcal{M}_T \mathcal{M}_\theta \mathcal{M}_D, \\ \mathcal{M}_T &= \text{diag} \left(e^{i\mathbf{K}_+^b \cdot \mathbf{r}}, e^{i\mathbf{K}_+^b \cdot \mathbf{r}}, e^{i\mathbf{K}_+^t \cdot \mathbf{r}}, e^{i\mathbf{K}_+^t \cdot \mathbf{r}} \right), \\ \mathcal{M}_\theta &= \text{diag} \left(e^{i\frac{\theta}{4}\sigma_z}, e^{i\frac{\theta}{4}\sigma_z}, e^{-i\frac{\theta}{4}\sigma_z}, e^{-i\frac{\theta}{4}\sigma_z} \right). \end{aligned} \quad (13)$$

The transformed Hamiltonian $h_1(\mathbf{r})$ reads:

$$h_1(\mathbf{r}) = \begin{pmatrix} -i\boldsymbol{\sigma} \cdot \boldsymbol{\nabla} & T_{0,\theta} & 0 & 0 \\ T_{0,\theta}^\dagger & -i\boldsymbol{\sigma} \cdot \boldsymbol{\nabla} & T_\theta(\mathbf{r}) & 0 \\ 0 & T_\theta^\dagger(\mathbf{r}) & -i\boldsymbol{\sigma} \cdot \boldsymbol{\nabla} & T_{0,\theta} \\ 0 & 0 & T_{0,\theta}^\dagger & -i\boldsymbol{\sigma} \cdot \boldsymbol{\nabla} \end{pmatrix} = \begin{pmatrix} 0 & -i\bar{\partial} & 0 & 0 & 0 & 0 & 0 & 0 \\ -i\bar{\partial} & 0 & t_\theta & 0 & 0 & 0 & 0 & 0 \\ 0 & t_\theta^* & 0 & -i\bar{\partial} & 0 & U_{-\phi} & 0 & 0 \\ 0 & 0 & -i\bar{\partial} & 0 & U_\phi & 0 & 0 & 0 \\ 0 & 0 & 0 & U_\phi^* & 0 & -i\bar{\partial} & 0 & 0 \\ 0 & 0 & U_{-\phi}^* & 0 & -i\bar{\partial} & 0 & t_\theta^* & 0 \\ 0 & 0 & 0 & 0 & 0 & t_\theta & 0 & -i\bar{\partial} \\ 0 & 0 & 0 & 0 & 0 & 0 & -i\bar{\partial} & 0 \end{pmatrix}, \quad (14)$$

where $T_{0,\theta} = \begin{pmatrix} 0 & 0 \\ t_\theta & 0 \end{pmatrix}$ and $t_\theta = \exp(i\theta/2)$. We next shuffle into the sublattice basis, and the Hamiltonian is brought into the off-diagonal form:

$$h_3(\mathbf{r}) = \begin{pmatrix} & \mathcal{D}_{2,\theta} \\ \mathcal{D}_{2,\theta}^\dagger & \end{pmatrix}, \quad \mathcal{D}_{2,\theta}^\dagger = \begin{pmatrix} -i\bar{\partial} & t_\theta & 0 & 0 \\ 0 & -i\bar{\partial} & U_\phi & 0 \\ 0 & U_{-\phi}^* & -i\bar{\partial} & t_\theta^* \\ 0 & 0 & 0 & -i\bar{\partial} \end{pmatrix}, \quad \mathcal{D}_{2,\theta} = \begin{pmatrix} -i\bar{\partial} & 0 & 0 & 0 \\ t_\theta^* & -i\bar{\partial} & U_{-\phi} & 0 \\ 0 & U_\phi^* & -i\bar{\partial} & 0 \\ 0 & 0 & t_\theta & -i\bar{\partial} \end{pmatrix}. \quad (15)$$

The θ dependence in t_θ can be further eliminated by a unitary rotation in the Dirac layers:

$$\mathcal{D}_2^\dagger \equiv \begin{pmatrix} e^{-i\theta/2} & 0 & 0 & 0 \\ 0 & 1 & 0 & 0 \\ 0 & 0 & 1 & 0 \\ 0 & 0 & 0 & e^{-i\theta/2} \end{pmatrix} \mathcal{D}_{2,\theta}^\dagger \begin{pmatrix} e^{i\theta/2} & 0 & 0 & 0 \\ 0 & 1 & 0 & 0 \\ 0 & 0 & 1 & 0 \\ 0 & 0 & 0 & e^{i\theta/2} \end{pmatrix}, \quad (16)$$

after which we arrive at the chiral-TDBG Hamiltonian used in the main text:

$$H_{n=2}(\mathbf{r}) = \begin{pmatrix} & \mathcal{D}_2 \\ \mathcal{D}_2^\dagger & \end{pmatrix}, \quad \mathcal{D}_2^\dagger = \begin{pmatrix} -i\bar{\partial} & t_1 & 0 & 0 \\ 0 & -i\bar{\partial} & U_\phi & 0 \\ 0 & U_{-\phi}^* & -i\bar{\partial} & t_1 \\ 0 & 0 & 0 & -i\bar{\partial} \end{pmatrix}, \quad \mathcal{D}_2 = \begin{pmatrix} -i\bar{\partial} & 0 & 0 & 0 \\ t_1 & -i\bar{\partial} & U_{-\phi} & 0 \\ 0 & U_\phi^* & -i\bar{\partial} & 0 \\ 0 & 0 & t_1 & -i\bar{\partial} \end{pmatrix}.$$

The multi-layer generalization of the above unitary transformations is straightforward, leading to the chiral model Hamiltonian,

$$H_n(\mathbf{r}) = \begin{pmatrix} & \mathcal{D}_n \\ \mathcal{D}_n^\dagger & \end{pmatrix}, \quad \mathcal{D}_n = \begin{pmatrix} \mathcal{D}_1 & t_1 T_+ & & & \\ t_1 T_- & h_D & t_2 T_+ & & \\ & t_2 T_- & h_D & \ddots & \\ & & \ddots & \ddots & \\ & & & t_{n-1} T_+ & \\ & & & t_{n-1} T_- & h_D \end{pmatrix}. \quad (17)$$

Intravalley Inversion

Here we show the details of $[\mathcal{I}, H_n] = 0$ where \mathcal{I} is the intravalley inversion operation:

$$\mathcal{I} = \begin{pmatrix} & \mathcal{P} \\ -\mathcal{P} & \end{pmatrix} \mathcal{K}, \quad \mathcal{P} = \text{diag}(\tau_y, -\tau_y, \dots, (-)^{n-1}\tau_y). \quad (18)$$

We first note that:

$$\mathcal{P}\mathcal{D}_n(\mathbf{r})\mathcal{P} = -(\mathcal{D}_n^\dagger(\mathbf{r}))^*, \quad \mathcal{P}\mathcal{D}_n^\dagger(\mathbf{r})\mathcal{P} = -\mathcal{D}_n^*(\mathbf{r}). \quad (19)$$

The derivation of Eqn. (19) can be seen as below:

$$\begin{aligned} \mathcal{P}\mathcal{D}_n\mathcal{P} &= \begin{pmatrix} \tau_y\mathcal{D}_1\tau_y & -t_1\tau_y T_+\tau_y & & & \\ -t_1\tau_y T_-\tau_y & \tau_y h_D\tau_y & -t_2\tau_y T_+\tau_y & & \\ & -t_2\tau_y T_-\tau_y & \tau_y h_D\tau_y & \ddots & \\ & & \ddots & \ddots & \\ & & & -t_{n-1}\tau_y T_+\tau_y & \\ & & & -t_{n-1}\tau_y T_-\tau_y & \tau_y h_D\tau_y \end{pmatrix}, \\ &= - \begin{pmatrix} \mathcal{D}_1^\dagger & t_1 T_- & & & \\ t_1 T_+ & h_D^\dagger & t_2 T_- & & \\ & t_2 T_+ & h_D^\dagger & \ddots & \\ & & \ddots & \ddots & \\ & & & t_{n-1} T_- & \\ & & & t_{n-1} T_+ & h_D^\dagger \end{pmatrix}^* = -[\mathcal{D}_n^\dagger]^*, \end{aligned} \quad (20)$$

where in the last line, we used the identity [15] following the $\mathcal{C}_2\mathcal{T}$ invariance of cTBG,

$$\tau_y D_1(\mathbf{r})\tau_y = -\mathcal{D}_1(-\mathbf{r}) = -[\mathcal{D}_1^\dagger(\mathbf{r})]^*, \quad \tau_y h_D(\mathbf{r})\tau_y = -h_D(-\mathbf{r}) = -[h_D^\dagger(\mathbf{r})]^*. \quad (21)$$

Therefore we can prove $[\mathcal{I}, H_n] = 0$ by using:

$$\begin{pmatrix} & \mathcal{P} \\ -\mathcal{P} & \end{pmatrix} \begin{pmatrix} & \mathcal{D}_n \\ \mathcal{D}_n^\dagger & \end{pmatrix} \begin{pmatrix} & \mathcal{P} \\ -\mathcal{P} & \end{pmatrix} = \begin{pmatrix} & -\mathcal{P}\mathcal{D}_n^\dagger\mathcal{P} \\ -\mathcal{P}\mathcal{D}_n\mathcal{P} & \end{pmatrix} = \begin{pmatrix} & \mathcal{D}_n \\ \mathcal{D}_n^\dagger & \end{pmatrix}^*. \quad (22)$$

Numerical Calculation of Band Geometries

In the main text, we have proved the band geometry of our model is ideal. This means that Berry curvature is positive and proportional to the Fubini-Study metric $\Omega_{\mathbf{k}} = \omega_{ab}g_{\mathbf{k}}^{ab}$. The right hand side defines the trace of the Fubini-Study metric.

The Berry curvature $\Omega_{\mathbf{k}}$ and the Fubini-Study metric $g_{\mathbf{k}}^{ab}$ are defined respectively as the imaginary and real part of the quantum geometric tensor,

$$\mathcal{Q}_{\mathbf{k}}^{ab} \equiv \langle D_{\mathbf{k}}^a u_{\mathbf{k}} | D_{\mathbf{k}}^b u_{\mathbf{k}} \rangle = g_{\mathbf{k}}^{ab} + \frac{i\epsilon^{ab}}{2}\Omega_{\mathbf{k}}, \quad (23)$$

where $|u_{\mathbf{k}}\rangle$ is the cell-periodic part of the Bloch wavefunction, $D_{\mathbf{k}}^a = \partial_{\mathbf{k}}^a - iA_{\mathbf{k}}^a$ is the covariant derivative with respect to the Berry connection $A_{\mathbf{k}}^a = -i\langle u_{\mathbf{k}} | \partial_{\mathbf{k}}^a u_{\mathbf{k}} \rangle$, and $\epsilon^{xy} = -\epsilon^{yx} = 1$ is the 2D anti-symmetric tensor.

In Fig. 4 we numerically verify the ideal band geometry for flatbands in our model for $n = 1, 2, 3$ which corresponds to cTBG, cTDBG and chiral twisted double tri-layer graphene (cTDTG), respectively. The numerical result verifies the ideal flatband condition Eq. (1) that the Berry curvature is non-vanishing, and proportional to the trace of the Fubini-Study metric.

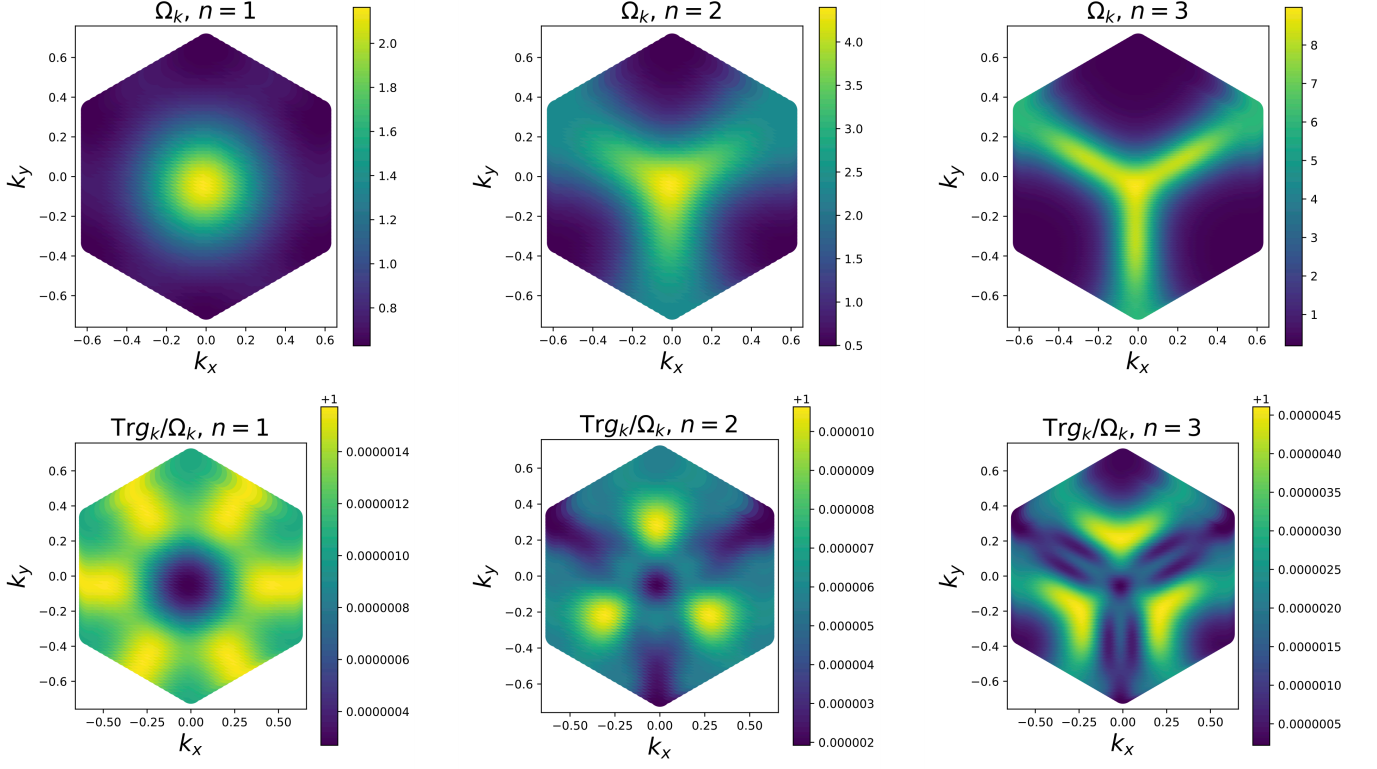


FIG. 4. The numerical data of Berry curvature (first row) and its ratio to the Fubini-Study metric $\text{Tr}g_{\mathbf{k}}/\Omega_{\mathbf{k}} = 1$ (second row), in the flatband of cTBG (first column), cTDBG (second column) and cTDTG (third column). The trace is defined as $\text{Tr}g_{\mathbf{k}} = \omega_{ab}g_{\mathbf{k}}^{ab}$ where ω_{ab} in our case is δ_{ab} . The numerical result verifies the ideal flatband condition Eq. (1) that the Berry curvature is non-vanishing, and proportional to the trace of the Fubini-Study metric. Small deviations to 1 of the second row are numerical artifacts due to finite momentum space grid in numerical calculations which goes to zero in the thermodynamic limit.

Details of Perturbation Analysis and the Wavefunction Exchange Mechanism

In this section, we work out the details of the basis wavefunctions used for the degenerate perturbation calculation discussed in the main text. For simplicity, we focus on $n = 2$ where the basis wavefunctions includes two Dirac wavefunctions and two cTBG flatband wavefunctions at the Moiré $\pm\mathbf{K}$ points. We start with considering interlayer coupling $t_1 = 0$. The Dirac Hamiltonian describing the outermost two layers written in the sublattice basis is given by:

$$H_D = \begin{pmatrix} \mu\tau_0 & -i\partial\tau_0 \\ -i\bar{\partial}\tau_0 & -\mu\tau_0 \end{pmatrix}, \quad (24)$$

where $\boldsymbol{\tau}$ is the layer Pauli matrix (representing the bottom-most and top-most layers), μ is the hexagonal-boron-nitride potential. At Moiré Dirac point $\pm\mathbf{K}$, its eigenstate wavefunction is a tensor product,

$$\Psi_D = \psi^\sigma \otimes \psi^\tau, \quad (25)$$

where ψ^σ is a sublattice spinor and ψ^τ is a layer spinor.

Note that because of the unitary transformation Eq. (13), the action of translations in the chiral basis is:

$$\mathcal{V}_{1,2}\psi_{\mathbf{k}}(\mathbf{r}) = e^{i\tau_z\mathbf{K}\cdot\mathbf{a}_{1,2}}\psi_{\mathbf{k}}(\mathbf{r} + \mathbf{a}_{1,2}) = e^{i(\mathbf{k}+\tau_z\mathbf{K})\cdot\mathbf{a}_{1,2}}\psi_{\mathbf{k}}(\mathbf{r}), \quad (26)$$

where $\tau_z = +1$ for the bottom layers, and $\tau_z = -1$ for the top n layers. Therefore the $\mathbf{k} = 0$ point corresponds to the Moiré \mathbf{K} point for the bottom n layers, and to the $-\mathbf{K}$ point for the top layers.

For this reason, ψ^τ has a simple form at Moiré Dirac points $\mathbf{k} = 0$ [written in basis of the (bom, top) layer]:

$$\psi_{\mathbf{k}}^\tau = \begin{cases} (1, 0)^T, & \text{for } \mathbf{k} = \mathbf{K} \\ (0, 1)^T, & \text{for } \mathbf{k} = -\mathbf{K} \end{cases} \quad (27)$$

Since ψ^τ is a simple layer spinor, we focus on the sublattice wavefunctions ψ^σ only. When $\mu = 0$, the eigen-energies and eigen-wavefunctions are:

$$\begin{aligned} E_- &= -|k|, & \psi_{-, \mathbf{k}}^\sigma &= \left(-\frac{|k|}{k}, +1 \right)^T, \\ E_+ &= +|k|, & \psi_{+, \mathbf{k}}^\sigma &= \left(+\frac{|k|}{k}, +1 \right)^T, \end{aligned}$$

which has a singularity at Dirac point $\mathbf{k} = 0$. The singularity can be removed by setting $\mu \neq 0$. With $k = (k_x + ik_y)/\sqrt{2}$ and $\bar{k} = (k_x - ik_y)/\sqrt{2}$, the eigen-energies and eigen-wavefunctions are:

$$\begin{aligned} E_- &= -\sqrt{|k|^2 + \mu^2}, & \psi_{-, \mathbf{k}}^\sigma &= \left(\frac{\mu - \sqrt{|k|^2 + \mu^2}}{k}, 1 \right)^T, \\ E_+ &= +\sqrt{|k|^2 + \mu^2}, & \psi_{+, \mathbf{k}}^\sigma &= \left(1, \frac{-\mu + \sqrt{|k|^2 + \mu^2}}{\bar{k}} \right)^T. \end{aligned} \quad (28)$$

Reducing to the Dirac point $\mathbf{k} = 0$, we get:

$$\begin{aligned} E_- &= -|\mu|, & \psi_{-, \mathbf{k}=0}^\sigma &= (0, 1)^T, \\ E_+ &= +|\mu|, & \psi_{+, \mathbf{k}=0}^\sigma &= (1, 0)^T, \end{aligned} \quad (29)$$

from which we see the positive (negative) energy state is completely sublattice-A (B) polarized.

Writing in the basis of (TBG-A, Dirac-A, TBG-B, Dirac-B), we get the Moiré \mathbf{K} point Dirac wavefunction as below:

$$\Psi_{\mathbf{D}}^+ = \begin{pmatrix} \mathbf{0} & \phi_{\mathbf{D}}^T & \mathbf{0} & \mathbf{0} \end{pmatrix}^T, \quad \Psi_{\mathbf{D}}^- = \begin{pmatrix} \mathbf{0} & \mathbf{0} & \mathbf{0} & \chi_{\mathbf{D}}^T \end{pmatrix}^T, \quad (30)$$

where $\phi_{\mathbf{D}} = \chi_{\mathbf{D}} = \begin{pmatrix} 1, 0 \end{pmatrix}^T$ is a layer spinor representing the bottom and top layer. The cTBG wavefunctions are sublattice polarized, so we can label them by:

$$\Psi_{\text{cTBG}}^+ = \begin{pmatrix} \phi_{\text{cTBG}}^T & \mathbf{0} & \mathbf{0} & \mathbf{0} \end{pmatrix}^T, \quad \Psi_{\text{cTBG}}^- = \begin{pmatrix} \mathbf{0} & \mathbf{0} & \chi_{\text{cTBG}}^T & \mathbf{0} \end{pmatrix}^T. \quad (31)$$

In the (TBG, Dirac) basis, the perturbation matrix H_T is given by,

$$H_T = \begin{pmatrix} & T \\ T^\dagger & \end{pmatrix}, \quad T = \begin{pmatrix} & T_+ \\ T_- & \end{pmatrix}, \quad (32)$$

where T_\pm are given in the main text. The H_T couples distinct sublattice, whose matrix elements in terms of $\Psi_{\mathbf{D}}^\pm$ and Ψ_{cTBG}^\pm are,

$$\langle \Psi_{\text{cTBG}}^+ | H_T | \Psi_{\mathbf{D}}^- \rangle = \langle \phi_{\text{cTBG}} | T_+ | \chi_{\mathbf{D}} \rangle \neq 0, \quad (33)$$

$$\langle \Psi_{\text{cTBG}}^- | H_T | \Psi_{\mathbf{D}}^+ \rangle = \langle \chi_{\text{cTBG}} | T_- | \phi_{\mathbf{D}} \rangle = 0, \quad (34)$$

and their Hermitian conjugates. Eqn. (33) and Eqn. (34) are the key results of this section, used in the main text to analyze the analytical property of the Bloch wavefunction when t_1 is nonzero.

Interacting Hamiltonian and Exact Fractional Chern Insulators

In momentum space, the many-body interaction is,

$$H = \sum_{\mathbf{q}} v_{\mathbf{q}} \rho_{\mathbf{q}} \rho_{-\mathbf{q}}, \quad (35)$$

$$v_{\mathbf{q}} = \sum_m \tilde{v}_m L_m(\mathbf{q}^2 \ell^2) \exp(-\mathbf{q}^2 \ell^2 / 2), \quad (36)$$

where $\rho_{\mathbf{q}}$ is the flatband projected density operator. The $v_{\mathbf{q}}$ can be expanded into Haldane's pseudopotentials according to Eq. (36) where L_m is the Laguerre polynomial and Laguerre-Gaussian functions are complete orthogonal basis. Here $2\pi\ell^2$ is the area of the Moiré unit cell. The H_{int} used in the main text corresponds to the model interaction $\tilde{v}_1 \neq 0$.

In this appendix, we comment on the effect of \tilde{v}_0 . For single layer fermionic (bosonic) system, only odd (even) components matter. For multi-layered system, both even and odd components influence the energy spectrum, as the inter-layer interaction is not constrained by the Pauli principle.

For layer-isotropic interaction, the finite energy spectrum dependent both on \tilde{v}_0 and \tilde{v}_1 , but the exact zero modes observed in Fig. 3 of the main text are unaffected regardless of $\tilde{v}_{0,1}$. We want to emphasize these exact FCIs are intrinsic to the outermost Dirac layer *i.e.* the ϕ_n component. We have checked that further projecting $\rho_{\mathbf{q}}$ into ϕ_n only affects the excited energies but retains the $(2n+1)$ -fold degenerate zero modes and gives identical ground-state PES. Furthermore, the energy spectrum of the ϕ_n layer projected interaction is independent on the v_0 pseudopotential implying the zero-energy ground states are purely spanned in the basis of ϕ_n , with a vanishing power of $2n+1$ when two electrons approach each other.